A Multiscale Optimization Approach to Detect Exudates in the Macula

Carla Agurto, *Member, IEEE*, Victor Murray, *Senior Member, IEEE*, Honggang Yu, *Member, IEEE*,
Jeffrey Wigdahl, *Member, IEEE*, Marios Pattichis, *Senior Member, IEEE*, Sheila Nemeth,
E. Simon Barriga, *Member, IEEE*, and Peter Soliz, *Member, IEEE*

Abstract—**Pathologies that occur on or near the fovea, such as clinically significant macular edema (CSME), represent high risk for vision loss. The presence of exudates, lipid residues of serous leakage from damaged capillaries, has been associated with CSME, in particular if they are located one optic disc-diameter away from the fovea. In this paper, we present an automatic system to detect exudates in the macula. Our approach uses optimal thresholding of instantaneous amplitude (IA) components that are extracted from multiple frequency scales to generate candidate exudate regions. For each candidate region, we extract color, shape, and texture features that are used for classification. Classification is performed using partial least squares (PLS). We tested the performance of the system on two different databases of 652 and 400 images. The system achieved an area under the receiver operator characteristic curve (AUC) of 0.96 for the combination of both databases and an AUC of 0.97 for each of them when they were evaluated independently.**

Index Terms—**Amplitude-modulation frequency-modulation, clinically significant macular edema (CSME), diabetic retinopathy, partial least squares (PLS).**

I. INTRODUCTION

A RECENT study from the Johns Hopkins University found an increase of 89% of people over 40 with diabetic retinopathy (DR) since 2000 [1]. The statistics suggest that DR is the leading cause of new blindness in the US, affecting 25.8 million people [1]. Clinically significant macular edema (CSME) is one of the main contributors of vision loss in diabetics, accounting for 75% of sight-threatening cases [2]. This condition, which can appear at any stage of DR, affects the macula, the region that contains most of the photoreceptors in the retina. In CSME, an incremental thickening of the macular area in the retina occurs due to the accumulation of fluid. Diagnosing

CSME requires stereo imaging or optical coherence tomography (OCT) imaging. However, it has been demonstrated that hard exudates located within a one disc diameter (DD) area centered in the fovea are surrogates for CSME [3]. By detecting cases with exudates in the macula and providing proper treatment, the risk of moderate vision loss decreases to 50%, according to the Early Treatment Diabetic Retinopathy Study (ETDRS) [4]. Thus, it is important to develop accurate methods for detecting the presence of exudates in the macula.

The detection of exudates in the retina has been an active area of research, with increased interest since 2000 [5]–[13]. One of the first published papers on exudate detection [5] relied on the use of global and local thresholding in green channel images. In [6], the authors used an image intensity threshold based on estimates of the background image intensity levels. In [9], the authors proposed the use of adaptive intensity thresholding combined with recursive region growing segmentation (RRGS). Other approaches are based on the application of morphological operations to detect contours of exudates [7], fuzzy c-means clustering candidates [8], [10], and combination of classifiers [13] to detect exudate pixels. A recently published approach presented a top-down approach [14]. In [14], the authors assess the severity of the disease by examining the symmetry of the macular region.

Overall, most of the methods used to detect exudates are based on thresholding techniques and a combination of classifiers. However, the direct application of thresholding on color spaces can be problematic due to significant spatial illumination variations. Thus, most techniques require contrast enhancement or illumination correction on the images prior to the application of thresholding. On the other hand, methods based on combinations of classifiers need to apply different classifier methods sequentially, which could potentially preclude their generalization capacity on databases different from the ones used on their studies. In addition, some of the approaches that apply combinations of classifiers also require the application of contrast enhancement to achieve better results.

More recent approaches include the use of multiscale approaches for lesion detection [8], [13], [15], [16]. Multiscale approaches for detecting microaneurysms are discussed in [15] and [16]. While it is true that some of these methods are used to detect exudates, they are usually used as features to be input to classification algorithms.

The proposed algorithm is based on multiscale amplitude-modulation frequency-modulation (AM-FM) representations, which have been shown to be robust and capable of detecting

several DR lesions with high accuracy [17], [18]. In AM-FM representations, illumination variations are captured in the instantaneous amplitude (IA). To avoid sensitivity to local illumination variations, instead of using fixed threshold values, the proposed approach determines percentiles of the IA histogram. The effectiveness of the approach is documented in the results' section, where ROC area of the final classification is shown to exceed 0.95. Thus, the proposed algorithm does not require the application of contrast enhancement nor illumination correction.

Our AM-FM approach represents the DR images using AM-FM components that are extracted at multiple scales. Within each scale, an optimal threshold is computed based on the detection performance over a training set.

We will demonstrate that our method achieves a good generalization capacity that does not require it to be trained with data from multiple databases. The significance of our approach here is that we train on one database while testing on a completely different database that does not originate from the same source. This is significantly different than most other approaches. In summary, the basic concepts in this paper that are different from prior work in this area (e.g., see [17] and [18]) include:

1) *A bottom-up classification approach to DR image analysis:* The paper uses a bottom-up approach starting with the classification of individual pixels as parts of exudates and then classifying images based on the exudates. This approach is fundamentally different from previous, top-down efforts that focused on classifying entire images without optimizing the feature selection process.

2) *A multiscale AM-FM approach for selecting exudate candidates in the macula:* An optimization approach is used for selecting components from different scales and combining them into a single component image. The current paper represents the first attempt at combining pixels from multiple scales to produce an estimate of the location of DR lesions.

3) *A hybrid approach that combines multiscale AM-FM methods with classical texture and shape features:* Multiscale AM-FM methods are only used for selecting exudate candidates. Once the exudate candidate regions have been selected, a collection of classical texture features (e.g., statistics from co-occurrence matrices) and shape descriptors are extracted and then used for characterizing the regions. Previous multiscale AM-FM efforts used AM-FM features (the histograms of the IA and the instantaneous frequency [IF]) for characterizing the different image regions.

4) *Good generalizability based on training from a limited, pre-segmented dataset without the need to retrain from a database from each collection site:* The current method is trained on a relatively small dataset of 52 images and tested on another 600 images from the same site and 400 images from another database. The results demonstrate excellent performance on both datasets. Thus, unlike prior research requiring training and testing on each dataset, the proposed method demonstrates better generalizability by giving excellent results on datasets that were collected from sites that were not included in the training set.
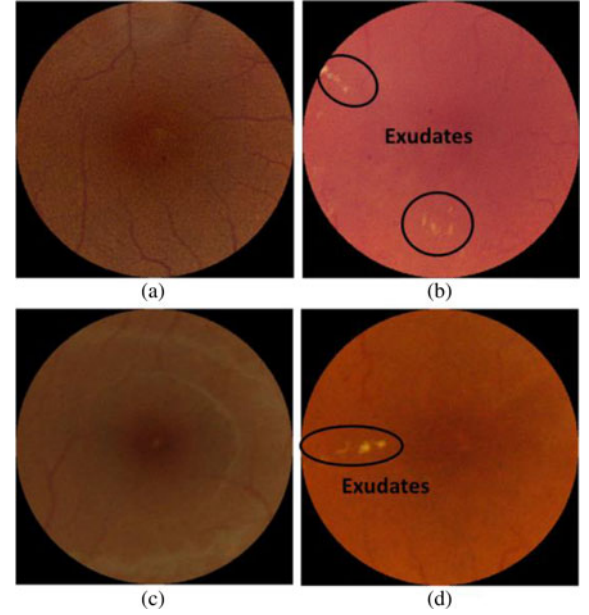

Fig. 1. Sample images. Maculae without exudates from (a) UTHSC SA and (c) MESSIDOR, and maculae with exudates from (b) UTHSC SA and (d) MESSIDOR.

TABLE I
DISTRIBUTION OF CASES IN THE TESTING DATASETS

Testing Sets	CSME cases	Normal	Total
UTHSC SA	166	434	600
MESSIDOR	84	316	400

The organization of this paper is as follows. Section II describes the data used to test the proposed approach. The methodology is explained in Section III. Results and discussion are presented in section IV. Concluding remarks are given in Section V.

II. DATA DESCRIPTION

Two databases were used to test our system. The first set of images was acquired at the University of Texas Health Science Center in San Antonio (UTHSC SA). The images were taken using a Canon CF-60 uv retinal camera with a 60° field of view (FOV). The size of the UTHSC SA images is 2048 × 2392 pixels. The second set of images was obtained from the publicly available MESSIDOR dataset [19]. These images were acquired at the Service d'Ophtalmologie, Hôpital Lariboisiere, Paris. Images were acquired using a 3CCD camera on a Topcon TRC NW6 retinograph with a FOV of 45. The size of the MESSIDOR images is 1488 × 2240 pixels.

Our dataset consists of 652 images from UTHSC SA, and 400 images from MESSIDOR. From the dataset of UTHSC SA, we selected 52 images to train the algorithm. Thus, we did not perform any training on the MESSIDOR database. Fig. 1 shows sample images in our datasets. Table I summarizes the number of CSME cases for each testing dataset. In order to apply the
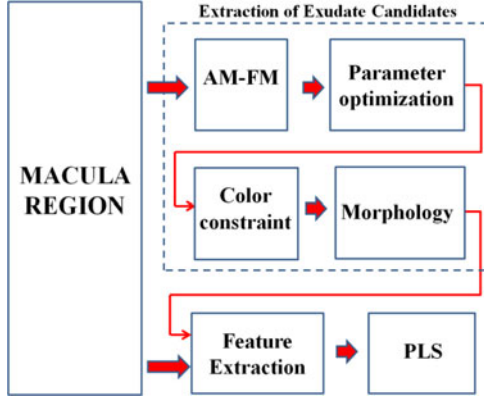
Fig. 2. Block diagram of the methodology used to detect exudates in the macula.
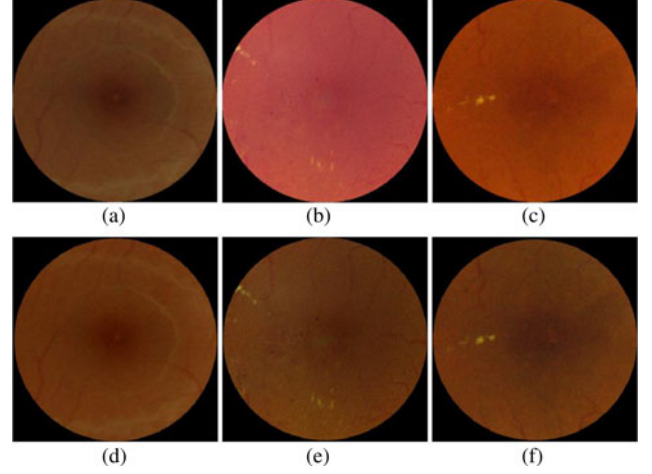

Fig. 3. Images after applying the normalization by shifting the mean value. Original images in (a), (b), and (c); and after normalization in (d), (e), and (f).

same classification model to the MESSIDOR images, the images from this dataset were resized to UTHSC SA dimensions.

III. METHODOLOGY

The methodology is summarized in Fig. 2. First, we select a circular region of interest (ROI) of radius of 200 pixels, which is approximately equivalent to one disc diameter (DD). AM-FM analysis is applied to the green channel of this ROI. Then, the extracted IAs are used for detecting lesion candidates. Lesion candidates are detected by applying an optimal threshold to the IA as described in the following section. Lesion candidates are also constrained to bright pixels, with noise removed using morphological operations. Features such as color from the RGB space, shape, and texture are obtained for each candidate (see Section III-F for details). Finally, candidate regions are classified as having exudates or as being exudate-free using partial least squares (PLS). In the following sections, we provide details on each processing block.

A. Preprocessing

The mean intensity value of each of the RGB channels was shifted so that all input images shared the same mean value [20]. This procedure standardizes the histograms of all the color channels, as their information will be used as features for the final classification of exudate candidates.

Fig. 3 shows our sample images as in Fig. 2 after the application of mean normalization. The differences in pigmentation in the normalized images [see Fig. 3(d)–(f)] are less noticeable than the ones observed in the original images [see Fig. 3(a)–(c)].

B. Amplitude-Modulation Frequency-Modulation

Multiscale AM-FM analysis decomposes an image in terms of a unique sum of IA and IF components given by

$$I(x,y) \approx \sum_{n=1}^{M} a_n(x,y) \cos \phi_n(x,y) \qquad (1)$$

where M is the number of frequency scales, $a_n(x,y)$ denote IA functions, and $\phi_n(x,y)$ denote the instantaneous phase

TABLE II
FREQUENCY SCALES FOR THE MULTISCALE AM-FM ANALYSIS

Frequency Bands	Instantaneous Period Range in mm
VL	0.064 to 0.176
L	0.032 to 0.088
M	0.016 to 0.044
H	0.008 to 0.022

functions [21]. The AM-FM estimates are obtained for $M = 4$ different frequency scales [22] which correspond to the following bands of frequencies: high (H), medium (M), low (L), and very low (VL). The size of exudates ranges between 0.015 and 0.055 mm. However, those smaller than 0.025 mm are invisible to fundus photography [23]. A summary of the frequency bands and its range in mm is given in Table II.

The IA estimates provide us with slow-varying (nontexture) intensity information of the structures presented in the image. This information is constrained by the bands of the frequency scale that is used. Thus, different frequency scales will capture structures with different characteristics.

In terms of the AM-FM component functions of equation (1), note that we restrict our attention to the use of the IA for exudate detection. In other words, we have not found that exudate detection can benefit from the use of IF features.

Fig. 4 shows an example of the extracted IAs for the four different scales. One can observe from the figure that exudates appear as high IA intensity in the VL, L, and M frequency scales. In contrast, there are no noticeable differences in intensity between the background and the exudates in the IA for the high-frequency scale [see Fig. 4(f)]. Furthermore, we have found this behavior to be typical for the images in our training set. As a result, in what follows, we do not consider the use of the IA from the high-frequency scales for exudate detection. We restrict our attention to the IA extracted from the VL, L, and M frequency scales since the lesions present components in those ranges.
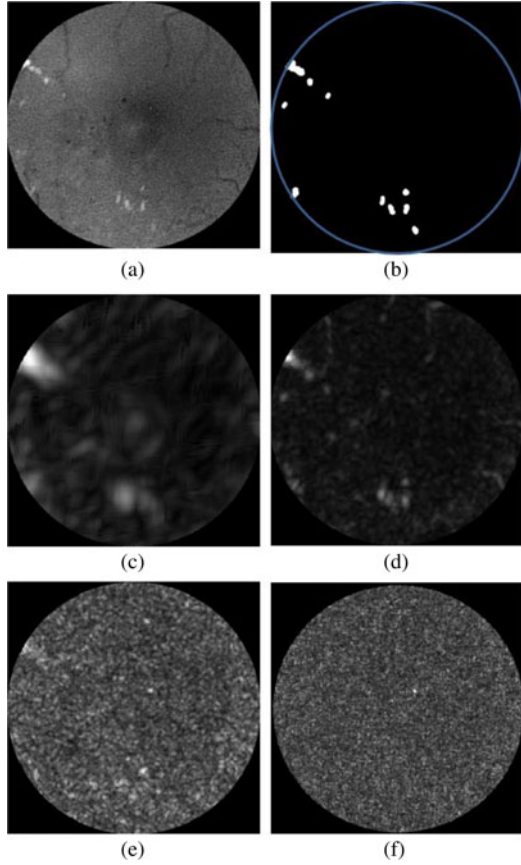
Fig. 4. Exudate representations in terms of the IA components. (a) Green channel of the original image, (b) manual segmentation of hard exudates in (a), IA estimates of (a) using (c) very low, (d) low-, (e) medium-, and (f) high-frequency scales.

C. Parameter Optimization

Exudates candidates are extracted by thresholding IA outputs on different frequency scales (VL, L, and M). To do so, we need to find the optimal threshold range, which is composed of lower and upper bound percentiles that are found by means of an iterative thresholding bound selection (ITBS). The metric that we used to find the optimal threshold range to extract exudate candidates is given by

$$\text{dist} = \sqrt{(1 - \text{sensitivity})^2 + (1 - \text{specificity})^2}, \quad (2)$$

where dist is the Euclidean distance from the operating point to the optimal point of sensitivity/specificity (sens/spec) equal to 100%/100%.

The procedure to obtain the optimal threshold range is explained as follows. The threshold range is initially set to [0th 100th] percentiles in the ITBS. Thus, initially, no pixels are excluded from being considered as exudate candidates. Then, the tree follows two branches: one increases the lower bound threshold by 1 percentile, while the other one decreases the upper bound by 1 percentile, yielding two binary maps in the following threshold ranges: [1st 100th] and [0th 99th], and the procedure is repeated until the optimal threshold range has been determined.
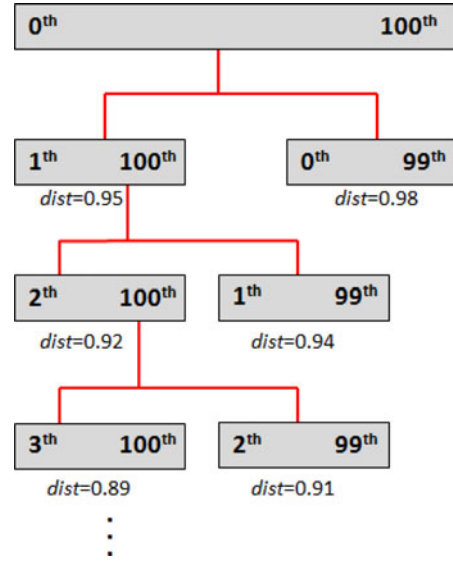

Fig. 5. ITBS of the optimization procedure for the extraction of exudate candidates.

The aforementioned procedure is applied to all 52 images in our training set. Each of these binary maps is compared to the reader-based ground truth for hard exudates, producing an operating point with values of sens/spec for each image. With this operating point, we calculate dist for each training image and its average value is computed.

In Fig. 5, the average dist values for the first two branches of the tree are 0.95 and 0.98. Since a low *dist* value indicates that the binary maps provide a better detection of the exudates, and brings us closer to the optimal point, the branch with dist = 0.95 is chosen.

In general, this procedure would be repeated until we reached the last branch at which *dist* achieved its lower value. In other words, the tree would be pruned once dist starts increasing. However, we do not want to do a candidate extraction that overfits the training data. To avoid doing so, we define thresh_dist, and the procedure is repeated only until we find the branch that achieves a minimum performance of dist = thresh_dist. The value of this parameter will determine the number of exudates candidates that the algorithm will extract. If the specified value for thresh_dist is high, more candidates, which are not necessarily exudates, will be extracted from each image. If the value for thresh_dist is low, the number of false positives among the candidates will be reduced, but the same could happen to the number of true positives. In other words, thresh_dist provides a method generalization tradeoff between the inclusion of all exudates and nonexudate structures.

To evaluate the performance of the algorithm, different values for thresh_dist were analyzed (see Table III). This procedure is applied independently to the three different frequency bands (VL, L, and M) to determine the optimal AM-FM threshold range. By performing the logical disjunction of the optimal binary maps in the three scales, the AM-FM candidates are obtained. If the ITBS of a specific frequency band does not achieve dist = thresh_dist, this band is not used for the extraction

TABLE III
RESULTS OF OPTIMAL RANGE FOR PERCENTILE THRESHOLDING
FOR IA SCALES

thresh_dist	IA-VL	IA-L	IA-M
0.15	-	-	-
0.20	-	[80 100]	[86 100]
0.25	[83 100]	[74 100]	[81 100]
0.30	[72 100]	[69 100]	[73 100]
0.35	[66 100]	[64 100]	[66 100]
0.40	[61 100]	[59 100]	[61 100]
0.45	[55 100]	[54 100]	[55 100]
0.50	[50 100]	[49 100]	[50 100]
0.55	[45 100]	[44 100]	[45 100]
0.60	[40 100]	[40 100]	[40 100]
0.65	[35 100]	[35 100]	[35 100]
0.70	[30 100]	[30 100]	[30 100]

Fig. 7. Candidates after green channel intensity constraint [see original image and its ground truth in Fig. 4(a) and (b)].

Fig. 8. Final step of the extraction of candidates using morphological operations [see original image and its ground truth in Fig. 4(a) and (b)].
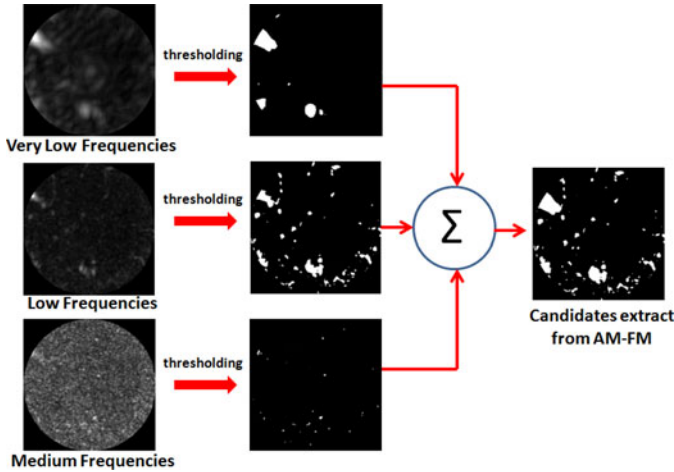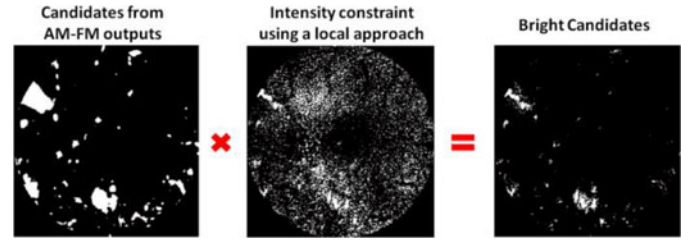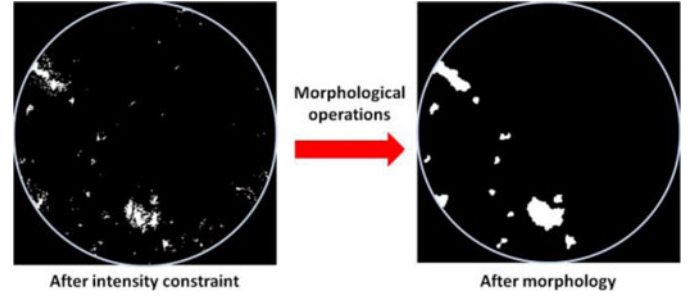

Fig. 6. Extraction of exudate candidates using AM-FM [see original image and its ground truth in Fig. 4(a) and (b)].

of candidates. It is also clear from the results in Table III that the optimization approach resulted in the selection of a single, low-value cutoff. In other words, high IA values resulted in the best exudate candidates.

In Fig. 6, we show the IA outputs of the reference image of Fig. 4, its thresholded images, and the AM-FM candidates obtained by following this approach. Note that the final image is generated as the union from the three scales.

D. Intensity Constraint

The methodology specified up to section C already extracts candidates that could be provided to the classifier to detect actual exudates. However, other structures such as vessels are also characterized by large IA values.

To reject the possibility of having unwanted structures from being considered as possible exudates, we constrain the candidate exudates to those pixels with large intensity values in the green channel. The additional constraint of requiring candidates

to be composed of bright pixels allows us to reject dark regions that may generate high IA values.

To select exudate candidates with bright pixels, we cannot apply global thresholding since an exudate's intensity varies depending on its location in the image. Hence, local thresholding is applied to the green channel by using a sliding window of 100 × 100 pixels, hereafter referred to as intensity thresholding. The pixels whose intensity is higher than a certain percentile of the content of this window will be preserved as bright pixels. The optimal intensity threshold is the one that achieves the minimum value of dist as outlined in the optimization example of Fig. 5.

In addition, we empirically set an intensity threshold in the foveal area to the 99th percentile of the macula content. This modification was implemented after noticing that exudates rarely appear in the center of the macula and that foveal reflex, a bright imaging artifact commonly present in retinal images, is darker than exudates. After this mask is generated, it is multiplied by the binary maps of exudate candidates, as shown in Fig. 7.

E. Morphology

In the final stage of the extraction of candidates, morphological dilation and erosion are applied with a circular structural element of radius 5 and 4 pixels respectively in order to group small candidates that are close to each other. In addition, we applied morphological close to remove noise by discarding candidates composed of less than N pixels (1 pixel has an area of 81 μm^2). We empirically set $N = 12$, which corresponds to an area smaller than the average size of a microaneurysm, which is the smallest pathology in DR. Fig. 8 shows the results after applying morphology.

F. Extraction of Features

Three types of features (color, shape, and texture) are extracted from each candidate to help differentiate the exudates from nonexudates structures.

Color image intensity features from the green and blue channels are extracted for each candidate and from their neighborhood pixels in normalized histograms of 16 bins each. We did not consider color information from the red channel. The red wavelengths penetrate deeper into the retina, reflecting mostly the choroidal depth, where exudates are not present. Additionally, the red channel intensity can be saturated. Therefore, we did not consider color features from the red channel, a common practice in both computer- and human-based retinal image analysis [24], [25].

Texture information for each candidate is obtained by using a gray level co-occurrence matrix (GLCM) [26] in the green channel. This matrix is calculated in a rectangular region. The region position and size is determined by the bounding box containing the candidate plus 10 pixels of margin. This matrix counts the number transitions between gray-scale values from two adjacent pixels. A total of four textural features (contrast, energy, homogeneity, and correlation) are obtained for each candidate using GLCM.

Shape properties are obtained from the pixels that are associated with each exudate candidate. The six shape features include: area estimated as the number of pixels that belong to the exudate candidate, the perimeter of the detected exudate candidate region, eccentricity, minor and major axis length, and solidity. The features in the training set are normalized to have zero mean and standard deviation 1. To do so, the mean and the standard deviation values are obtained for each of the features. These two estimates are stored and later used to normalize the features in the two testing sets.

G. Classification

The choice for optimal classifier depends on the size of the dataset. For small training sets, high bias/low variance classifiers (e.g., naive Bayes) can be used. However, in this case, the dataset is large since each candidate can be treated as a data sample. Thus, for the current application, low bias/high variance algorithms [e.g., k-nearest neighbors (kNN) or regression] are preferred as there is enough data to avoid overfitting and generate accurate models. SVM algorithms also provide high accuracy but they work better when there is a high dimensional feature representation of the data. A regression classifier, called PLS [27], was chosen since it also provides a probabilistic interpretation and the possibility of adjusting classification thresholds.

PLS is a linear regression method formulated as $y = X\beta + \varepsilon$, where y is a $n \times 1$ vector with the class information, X is a $n \times p$ matrix of the extracted features (n candidates $\times$ p features), β is a $p \times 1$ vector of regression coefficients, and ε is a $n \times 1$ vector of residuals. The SIMPLS algorithm [27] is used to obtain the regression coefficients.

The features obtained in Section III-F (32 color, 4 textural, and 6 shape) for each candidate extracted from the 52 images
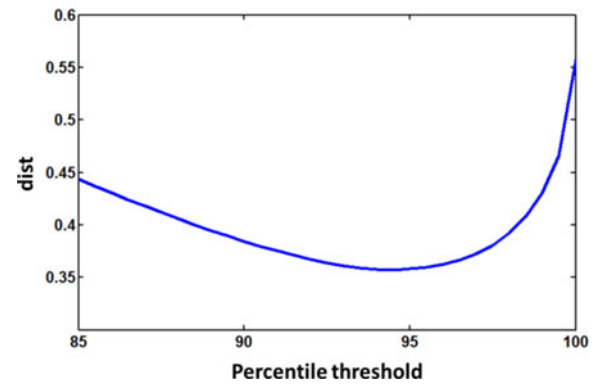

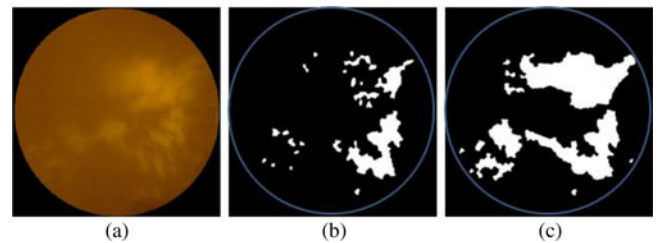Fig. 9. Curve of dist versus percentile threshold to obtain the optimal value for intensity constraint.

Fig. 10. Examples of the extraction of candidates for two values of thresh_dist: 0.20 and 0.70. (a) Original image. (b) Candidates obtained with thresh_dist = 0.20; (c) candidates obtained with thresh_dist = 0.70.

selected for training purposes from the UTHSC SA dataset are input to PLS. After finding the optimal regression coefficients, these are stored to be applied to the features extracted from the testing datasets.

IV. RESULTS AND DISCUSSION

A. Parameter Optimization

As discussed earlier, Table III provides the range of optimal percentile AM-FM thresholds for each thresh_dist in each scale of IA. Note that when the value of thresh_dist decreases, the range of percentile thresholds is increased, since less information is removed.

B. Intensity Constraint

The optimal intensity threshold is the one that achieves the minimum value of dist. Fig. 9 shows the plot of *dist* versus *percentile threshold*. In this graph, the minimum distance is found for the 94.5th percentile. This value was then used for thresholding all the images in the dataset.

C. Classification

Table IV shows the number of candidates used to train the algorithm for each *thresh_dist* value. It can be observed from this table that, initially, the number of candidates increases along with the value of thresh_dist, indicating that more candidates that actually include exudates are detected. The number starts to decrease as candidates that are close to each other combine when the percentile range is increased (see Fig. 10).

TABLE IV
NUMBER OF CANDIDATES IN THE TRAINING STAGE COMPOSED OF 52 IMAGES

thresh_dist	Exudates Candidates	Non-exudates Candidates
0.20	378	1406
0.25	399	2082
0.30	399	2375
0.35	393	2548
0.40	387	2614
0.45	387	2671
0.50	383	2661
0.55	380	2617
0.60	378	2576
0.65	377	2525
0.70	375	2496

TABLE V
AUC FOR THE CLASSIFICATION OF THE TESTING SETS

thresh_dist	Only UTHSC SA (600 images)	Only MESSIDOR (400 images)	UTHSC SA + MESSIDOR (1000 images)
0.20	0.969	0.960	0.957
0.25	**0.970**	**0.973**	**0.962**
0.30	0.969	0.972	0.959
0.35	0.966	0.970	0.955
0.40	0.966	0.973	0.958
0.45	0.967	0.966	0.956
0.50	0.967	0.964	0.955
0.55	0.968	0.963	0.957
0.60	0.967	0.964	0.957
0.65	0.968	0.963	0.957
0.70	0.968	0.964	0.957

Here, the focus is to detect the presence of exudates located within one disc diameter of the fovea. To evaluate the performance of the algorithm in the detection of those lesions, we generate a sensitivity/specificity ROC curve per image. To do so, the operating points of the ROC curve obtained for lesion detection in the training set is used to set the operating points for exudate detection on the testing set.

An image is considered to have exudates if at least one candidate is classified as an exudate. Table V shows the AUC of the two datasets evaluated as two independent test sets and jointly as a single test set. We notice that the results are similar among the different thresh_dist values. For the UTHSC SA cases, we have a small difference across these values, which may be due to our training set being composed exclusively by images from this database; a higher variation can be seen in the AUC values obtained by MESSIDOR for different thresh_dist values. Nonetheless, these AUC values are consistently high.
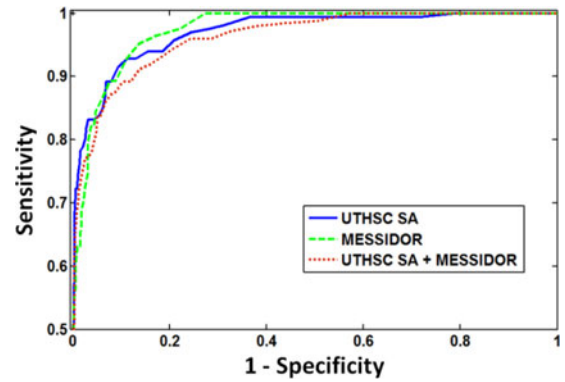

Fig. 11. ROC curves of the classification of CSME using thresh_dist = 0.25 for the two testing datasets evaluated both independently and jointly.

TABLE VI
SENSITIVITY/SPECIFICITY ACCURACY FOR THRESH_DIST = 0.25

Category	Only UTHSC SA (600 images)	Only MESSIDOR (400 images)	UTHSC SA + MESSIDOR (1000 images)
High Sensitivity	0.99/0.64 - 0.74	1.00/0.73 - 0.79	0.98/0.62 – 0.71
High Specificity	0.76/0.99 - 0.92	0.70/0.98 - 0.92	0.73/0.99 – 0.92
Highest Accuracy	0.83/0.97 - 0.93	0.82/0.96 - 0.93	0.77/0.97 – 0.92

When the testing dataset is composed of the 400 images from MESSIDOR and 600 images from UTHSC SA, the AUC decreases by 1% but the best result is still high with AUC = 0.96 (See red ROC curve in Fig. 11).

A more detailed analysis for the best result obtained with thresh_dist = 0.25 is described in Table VI. This table summarizes the results of three operating points in the ROC curves, where high sensitivity, high specificity, and high accuracy are obtained.

By selecting the operating point for high sensitivity in the UTHSC SA database, one image with exudates was not detected. This false-negative case is shown in Fig. 12(a). It is clear in the zoomed area shown in Fig. 12(b) that the exudates were subtle and difficult to visually distinguish. Although the algorithm missed these exudates, due to their focal minimal presence, they are not considered clinically significant. Fig. 12 also shows cases incorrectly classified as CSME (false positives). The most common case is the one presented in Fig. 12(c), where bright drusen are present in the macula. Another misclassified image is presented in Fig. 12(d), where retinal depigmentation caused the system to fail. Retinal depigmentation can be similar in tone to paler exudates.

Fig. 13 shows cases where exudates are clinically significant and the algorithm classifies them correctly. Similarly, Fig. 14 shows cases with exudates that are very challenging to detect. Here, the proposed algorithm is able to detect some of the present exudates and classify the image as abnormal.

As mentioned in the introduction section, the method proposed in [14] presented a top-down approach to detect exudates in a retinal image. This method was evaluated in the same MESSIDOR database. In their method, a large ROI area of 2DD is selected, obtaining AUC = 0.96 for all the 400 images. It also
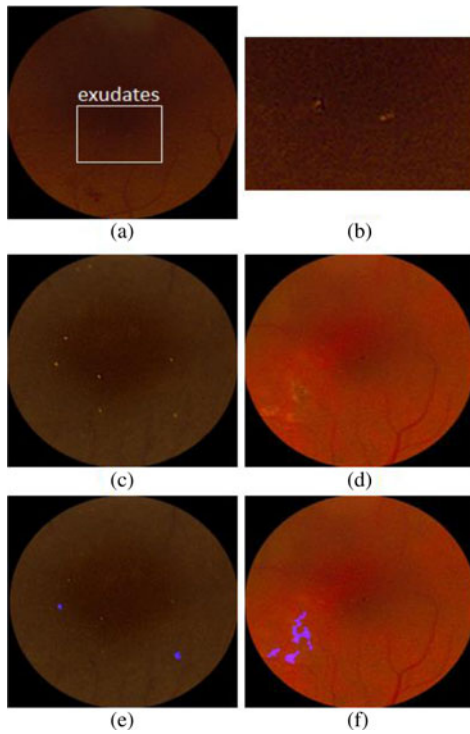
Fig. 12. Incorrectly classified maculae images. (a) CSME case and its zoomed region in (b), normal maculae in (c) and (d) and their classification results in (e) and (f), respectively. Pathologies in (b), (c), and (d) were enhanced for better visualization purposes.
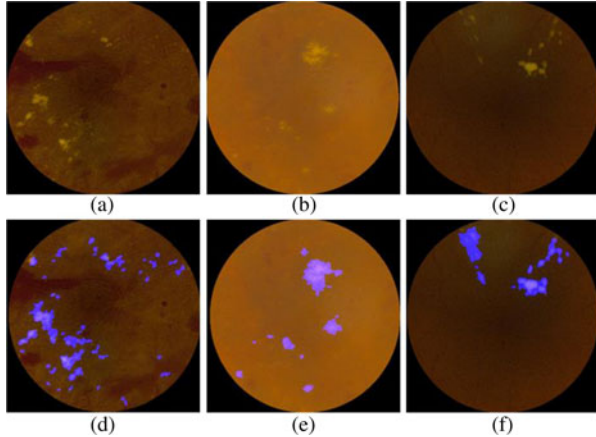

Fig. 13. Correctly classified CSME cases in the UTHSC SA database. Original images in (a), (b), and (c) and their classification results in (d), (e), and (f).
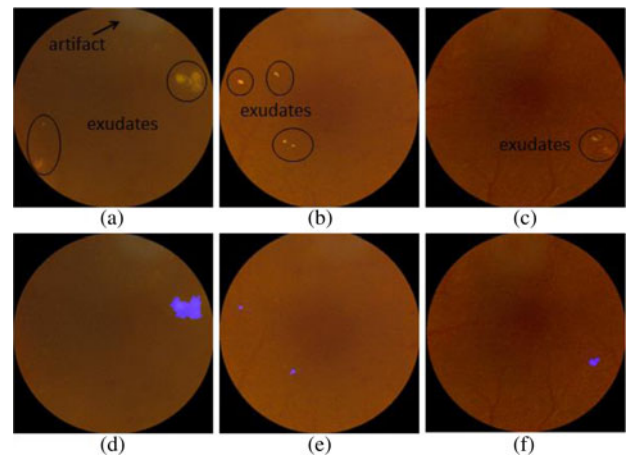

Fig. 14. Subtle cases of CSME in the UTHSC SA database that were correctly classified by the algorithm. Original images in (a), (b), and (c) and their classification results in (d), (e), and (f). Pathologies in (a), (b), and (c) were enhanced for better visualization purposes.
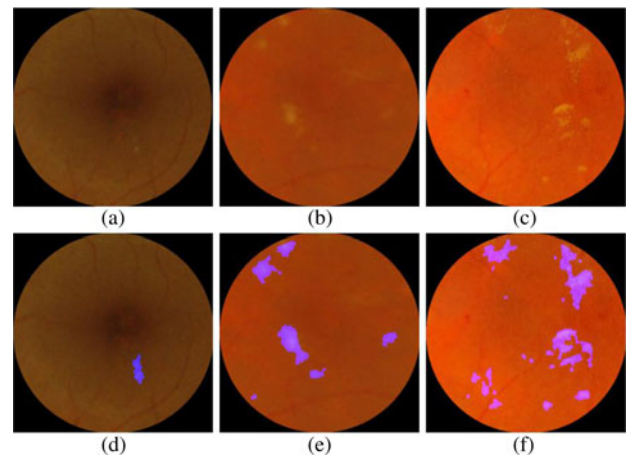

Fig. 15. Correctly classified CSME cases in the MESSIDOR database. Original images in (a), (b), and (c) and their classification result in (d), (e), and (f).

detects cases with CSME in a reduced set of the 400 images of MESSIDOR obtaining AUC of 0.99. However, they used the same ROI size, which usually contains larger clusters of exudates and are not in the area of definition of CSME. Although a direct comparison with this approach cannot be performed since we used all the 400 images, our result of AUC = 0.97 for CSME cases in MESSIDOR is high.

In the same paper, the MESSIDOR images are combined with other datasets, which reduced their overall performance to AUC = 0.92. In contrast, our results obtained by combining MESSIDOR with UTHSC SA data are only reduced to AUC = 0.96. In addition, our method does not require training in different datasets as they do, making our method potentially more robust and more likely to be applied in clinical practice. Fig. 15 shows three CSME cases correctly classified in MESSIDOR by our algorithm.

A large scale audit of the automated grading for DR was performed by Fleming *et al.* [28]. In their study 33535 patietns were screened obtaining 97.3% of sensitivity for patients with referable maculopathy (based on specificity = 49.6%). This value was adequate to conclude that the automated grading should be included in the Scotland's DR screening program. Our results are comparable to the ones obtained in [28], which suggest that our results are appropriate for an automatic DR screening setting.

A GPU accelerated version of the multiscale AM-FM analysis method used in the paper has been reported in [29]. Exudate detection requires approximated 12 s on an Intel Xeon Processor W3520 (CPU) running at 2.67 GHz, with 6 GB of memory with NVIDIA GeForce GTX465 card with 1 GB of global memory and 352 CUDA cores running at 607 MHz. We believe that this amount of time will be acceptable in a clinical setting where each exam will require several minutes.

V. CONCLUSION

This paper presents a novel method for detecting exudates in the macula. The algorithm shows robustness, since it did not require retraining when it was tested with a second dataset, the MESSIDOR dataset, obtaining an AUC with high sensitivity/specificity of 100%/73%.

Although the feature extraction and the classifier are important parts of the system, the extraction of candidates is the most important innovation. This system provides a reliable method for extraction of candidates without the need for applying contrast enhancement methods [8], [10] that may enhance the low-intensity noise of the images or extracting multiple features for classifiers to be able to detect candidates [8], [13].

In addition, we found that the fewer candidates obtained with low values of thresh_dist give us slightly better results in AUC per image classification than high values of thresh_dist. These results agree with previously published papers in DR screening systems [30], [31] in the sense that it is not necessary to detect every pixel of a DR lesion in order to detect with high sensitivity the presence of lesions in a retinal image.

This system can be used as a part of an automatic DR screening algorithm to ensure that no sight-threatening conditions due to the presence of exudates in the macula are missed.

ACKNOWLEDGMENT

REFERENCES

[1] Prevent Blindness America and National Eye Institute. Vision Problems in the U.S.: Prevalence of Adult Vision Impairment and Age-Related Eye Disease in America, 2012. Available: http://www.visionproblemsus.org/index.html

[2] F. K. Sutter, M. C. Gillies, and H. Helbig, "Diabetic macular edema:Current treatments," in *Medical Retina, ser. Essentials in Ophthalmology*, F. Holz and R. Spaide, Eds. Berlin Heidelberg: Springer, 2007, pp. 131–146.

[3] S. Resnikoff, D. Pascolini, D. Etyáale, I. Kocur, R. Pararajasegaram, G. P. Pokharel, and S. P. Mariotti, "Global data on visual impairment in the year 2002," *Bull. World Health Organ.*, vol. 82, pp. 844–851, 2004.

[4] Early Treatment Diabetic Retinopathy Study Research Group, "Photocoagulation for diabetic macular edema," *Arch. Ophthalmol.* vol. 103, no. 12, pp. 1796–1806, Dec. 1985.

[5] R. Phillips, J. Forrester, and P. Sharp, "Automated detection and quantification of retinal exudates," *Graefe's Arch. Clin. Exp. Ophthalmol.*, vol. 231, pp. 90–94, 1993.

[6] B. Ege, O. Hejlesen, O. Larsen, K. Moller, B. Jennings, D. Kerr, and D. Cavan, "Screening for diabetic retinopathy using computer based image analysis and statistical classification," *Comput. Meth. Programs Biomed.*, vol. 62, pp. 165–175, 2000.

[7] T. Walter, J. C. Klein, P. Massin, and A. Erginay, "A contribution of image processing to the diagnosis of diabetic retinopathy-detection of exudates in colour fundus images of the human retina," *IEEE Trans. Med. Imag.*, vol. 21, no. 10, pp. 1236–1243, Oct. 2002.

[8] A. Osareh, M. Mirmehdi, B. Thomas, and R. Markham, "Automated identification of diabetic retinal exudates in digital colour images," *Brit. J. Ophthalmol.*, vol. 87, pp. 1220–1223, 2003.

[9] D. Usher, M. Dumskyj, M. Himaga, T. H. Williamson, S. Nussey, and J. Boyce, "Automated detection of diabetic retinopathy in digital retinal images: A tool for diabetic retinopathy screening," *Diabetic Med.*, vol. 21, no. 1, pp. 84–90, 2004.

[10] A. Sopharak and B. Uyyanonvara, "Automatic exudates detection from diabetic retinopathy retinal image using fuzzy c-means and morphological methods," in *Proc. 3rd IASTED Int. Conf. Adv. Comput. Sci. Technol.*, Phuket, Thailand, 2007, pp. 359–364.

[11] A. D. Fleming, S. Philip, K. A. Goatman, G. J. Williams, J. A. Olson, and P. F. Sharp, "Automated detection of exudates for diabetic retinopathy screening," *Phys. Med. Biol*, vol. 52, pp. 7385–7396, 2007.

[12] C. I. Sanchez, M. Garcia, A. Mayo, M. I. Lopez, and R. Hornero, "Retinal image analysis based on mixture models to detect hard exudates," *Med. Image Anal.*, vol. 13, pp. 650–658, 2009.

[13] M. Niemeijer, S. R. Russell, M. A. Suttorp, B. van Ginneken, and M. D. Abràmoff, "Automated detection and differentiation of drusen, exudates, and cotton-wool spots in digital color fundus photographs for early diagnosis of diabetic retinopathy," *Invest. Ophthalmol. Vis. Sci.*, vol. 48, no. 5, pp. 2260–2267, 2007.

[14] K. S. Deepak and J. Sivaswamy, "Automatic assessment of macular edema from color retinal images," *IEEE Trans. Med. Imag.*, vol. 31, no. 3, pp. 766–776, Mar. 2012.

[15] G. Quellec, M. Lamard, P. M. Josselin, G. Cazuguel, B. Cochener, and C. Roux, "Optimal wavelet transform for the detection of microaneurysms in retina photographs," *IEEE Trans. Med. Imag.*, vol. 27, no. 9, pp. 1230–1241, Sep. 2008.

[16] B. Zhang, X. Wu, J. You, Q. Li, and F. Karray, "Detection of microaneurysms using multi-scale correlation coefficients," *Pattern Recog.*, vol. 43, no. 6, pp. 2237–2248, 2010.

[17] C. Agurto, V. Murray, E. Barriga, S. Murillo, M. S. Pattichis, H. Davis, S. Russell, M. D. Abramoff, and P. Soliz, "Multiscale AM-FM methods for diabetic retinopathy lesion detection," *IEEE Trans. Med. Imag.*, vol. 29, no. 2, pp. 502–512, Feb. 2010.

[18] C. Agurto, E. S. Barriga, V. Murray, S. Nemeth, R. Crammer, W. Bauman, G. Zamora, M. S. Pattichis, and P. Soliz, "Automatic algorithm for detection of diabetic retinopathy pathologies," *Invest. Ophthalmol. Vis. Sci.*, vol. 52, no. 8, pp. 5862–5871, 2011.

[19] TECHNO-VISION Project. *Messidor: Methods to evaluate segmentation and indexing techniques in the field of retinal ophthalmology*. (2004). [Online]. Available: http://messidor.crihan.fr/

[20] R. C. Gonzales and R. E. Woods, *Digital Image Processing*, 2nd ed.: NJ, USA: Prentice Hall, 2002.

[21] J. P. Havlicek, "AM-FM image vmodels," Ph.D. dissertation, The University of Texas at Austin, USA, 1996.

[22] V. Murray, P. Rodriguez, and M. S. Pattichis, "Multi-scale AM-FM demodulation and reconstruction methods with improved accuracy," *IEEE Trans. Image Process.*, vol. 19, no. 5, pp. 1138–1152, May 2010.

[23] J. J. Kanski, *Clinical Ophthalmology: A Systematic Approach*, 5th ed. Philadelphia, PA, USA: Butterworth/Heinemann/Elsevier, 2007.

[24] N. M. Salem and A. K. Nandi, "Novel and adaptive contribution of the red channel in pre-processing of colour fundus images," *J. Franklin Inst.*, vol. 344, pp. 243–256, 2007.

[25] M. E. Tyler, L. D. Hubbard, K. Boydston, and A. Pugliese, "Characteristics of digital fundus camera systems affecting tonal resolution of color retinal images," *J Ophthalmic Photogr.*, vol. 31, no. 1, pp. 9–14, 2009.

[26] R. M. Haralick, K. Shanmugan, and I. Dinstein, "Textural features for image classification," *IEEE Trans. Syst., Man, Cybern.*, vol. SMC-3, no. 6, pp. 610–662, Nov. 1973.

[27] S. de Jong, "SIMPLS: An alternative approach to partial least squares regression," *Chemometrics Intell. Lab. Syst.*, vol. 18, pp. 251–263, 1993.

[28] A. D. Fleming, K. A. Goatman, S. Philip, G. J. Prescott, P. F. Sharp, and J. A. Olson, "Automated grading for diabetic retinopathy: A large-scale audit using arbitration by clinical experts," *Brit. J. Ophthalmol.*, vol. 94, no. 12, pp. 1606–1610, 2010.

[29] C. Carranza, V. Murray, M. S. Pattichis, and E. S. Barriga, "Multiscale AM-FM decompositions with GPU acceleration for diabetic retinopathy screening," in *Proc. 2012 IEEE Southwest Symp. Image Anal. Interpretation (SSIAI)*, 2012, pp. 121–124.

[30] J. H. Hipwell, F. Strachan, J. A. Olson, K. C. McHardy, P. F. Sharp, and J. V. Forrester, "Automated detection of microaneuryms in digital red-free photographs: A diabetic retinopathy screening tool," *Diabetic Med.*, vol. 17, no. 8, 2000.

[31] M. Niemeijer, B. V. Ginneken, J. Staal, M. S. A. Suttorp-Schulten, and M. D. Abràmoff, "Automatic detection of red lesions in digital color fundus photographs," *IEEE Trans. Med. Imag.*, vol. 24, no. 5, pp. 584–592, May 2005.